PROCEEDINGS OF SPIE

SPIEDigitalLibrary.org/conference-proceedings-of-spie

Status of the SALTO demonstrator: project overview and first on-sky operations

G. Orban de Xivry, J. Paul, O. Absil, C. Adam, P. Albart, et al.

G. Orban de Xivry, J. Paul, O. Absil, C. Adam, P. Albart, C. Bastin, A. Boulanger, J. de Ville, E. Gabriel, L. Méant, V. Moreau, S. Orban, P. Remacle, F. Languy, M. Georges, J.-F. Vandenrijt, G. Millou, C. Nigot, V. Caramia, "Status of the SALTO demonstrator: project overview and first on-sky operations," Proc. SPIE 12185, Adaptive Optics Systems VIII, 1218534 (29 August 2022); doi: 10.1117/12.2627936

SPIE.

Event: SPIE Astronomical Telescopes + Instrumentation, 2022, Montréal, Québec, Canada

Status of the SALTO demonstrator: project overview and first on-sky operations

G. Orban de Xivry[a], J. Paul[a], O. Absil[a], C. Adam[b], P. Albart[b], C. Bastin[b], A. Boulanger[b], J. de Ville[b], E. Gabriel[b], L. Méant[b], V. Moreau[b], S. Orban[b], P. Remacle[b], F. Languy[c], M. Georges[c], J.-F. Vandenrijt[c], G. Millou[c], C. Nigot[d], and V. Caramia[d]

[a]Space sciences, Technologies, and Astrophysics Research (STAR) Institute, Université de Liège, Belgium
[b]Advanced Mechanical and Optical System (AMOS), Liège, Belgium
[c]Centre Spatial de Liège (CSL), Université de Liège, Belgium
[d]Redu Space Services (RSS), Redu, Belgium

ABSTRACT

The SALTO demonstrator is a complete 1-m class telescope with a single-conjugated Rayleigh laser guide star adaptive optics (AO) system. The project aims to benchmark robust AO operations for astronomy giving an opportunity to upgrade medium size telescopes (1-4 m diameter) around the world and boost their scientific yield. But it is also a benchmark for optical communications and space debris tracking under mediocre seeing conditions, far worse than astronomical standards. Indeed, the foreseen location of the telescope is at the premises of Redu Space Services in the Belgian countryside. In our contribution, we review the overall design of the AO instrument from the optical definition to the real-time computer implementation. We discuss the integration, the calibration, and operational aspects of the instrument. Finally, we present the successful first on-sky operations, reaching the diffraction limit at 1.55µm under 2-3" seeing.

Keywords: adaptive optics; telescope demonstrator; Rayleigh laser guide star

1. INTRODUCTION

One of the key driver for the SALTO project is to upgrade the large number of existing 1-4 m class telescopes. Indeed, laser-guided single conjugated adaptive optics (AO) system can greatly enhance the scientific capabilities of medium size telescopes, if they focus on scientific objectives that are hardly accessible on larger ones. The Robo-AO initiative has been very successful in following this route by providing, e.g., very efficient follow-up of large surveys like Kepler (e.g. 1). Several avenues, including and beyond conventional adaptive optics, are discussed in 2.

One of the central idea of SALTO is also to demonstrate robust LGS-AO operation in challenging conditions, such as in the Belgian countryside that offers only mediocre seeing conditions. Robustness and, by extension, automation is paramount to maximize the science return of AO system on medium size telescope, where AO observations are likely to be carried by non-AO experts (if not completely performed automatically) and to be able for example to carried out the follow-up of large surveys. But it is also of interest for optical ground stations (OGS) foreseen for ground-space optical telecommunications. Indeed, such OGS terminals are and will be typically deployed close to sea level, such as at Redu Space Services for SALTO, far from astronomical standard conditions. Hence one can expect much degraded seeing conditions, without mentioning possible daytime operations. Finally, small optical station with LGS-AO and fast-tracking capabilities are relevant for space awareness by boosting the ability of tracking and imaging space debris.

In this proceeding, we present the status of the SALTO project. We first provide a system overview including telescope and laser launch system but with an emphasis on the AO system. We then present our implementation of the real-time software, and the various calibration and wavefront control strategies that we have implemented. We then shortly present the first on-sky operations and future prospects for the project.

Further author information: (Send correspondence to G. Orban de Xivry)
G. Orban de Xivry: E-mail: gorban@uliege.be, Telephone: +32 4 3669712

Adaptive Optics Systems VIII, edited by Laura Schreiber, Dirk Schmidt, Elise Vernet,
Proc. of SPIE Vol. 12185, 1218534 · © 2022 SPIE
0277-786X · doi: 10.1117/12.2627936

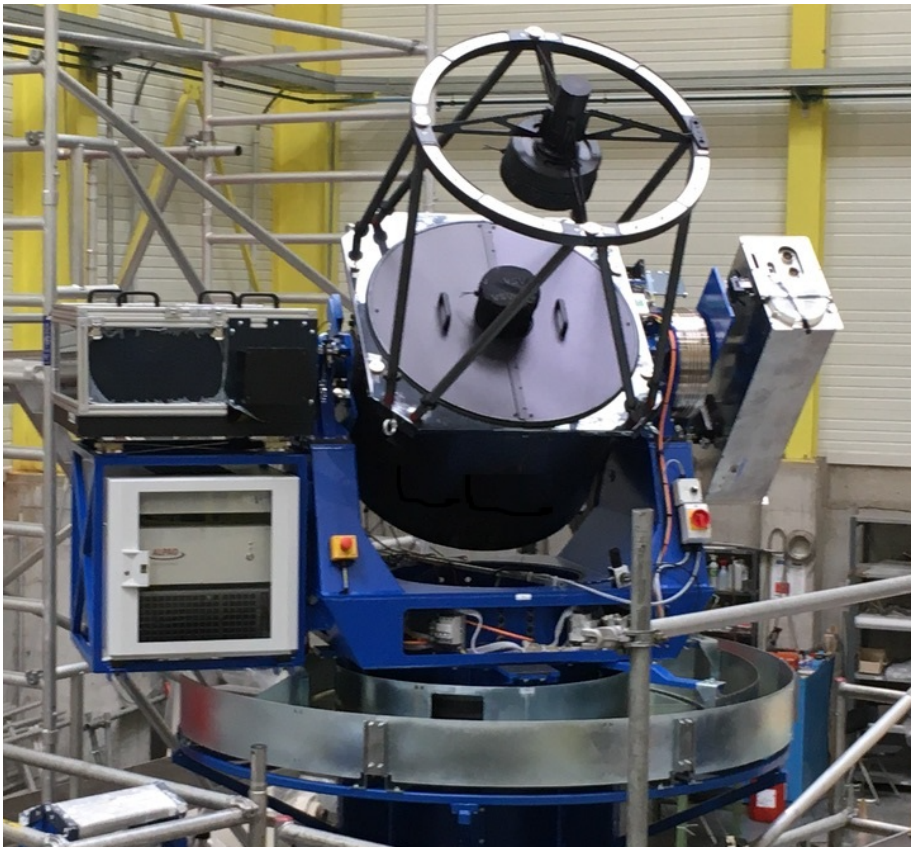

Figure 1. The SALTO demonstrator in the final phase of its integration at AMOS. On the left, the Nasmyth platform supporting the AO system. On the right, the laser system mounted on the altitude axis.

2. SALTO SYSTEM OVERVIEW

2.1 Telescope

The SALTO telescope is based on a Ritchey-Chrétien design with a 800mm aperture, 35% central obscuration, and has a f-number of 7.5. It has a M1 enhanced aluminium coating for optimal reflection in the visible, thin 2mm spiders, and a M2 focuser. The M1 mirror has a very good optical quality with ≤ 24 rms WFE. The tube is mounted on a custom fork, specifically designed by AMOS, that supports the heavy load from the Nasmyth AO instrument as well as the laser system mounted on the other side on the altitude axis. Hence thanks to the robustness of its mechanics, this "small" telescope can support such a complex and relatively heavy experimental setup. The complete telescope in AMOS' integration hall, including AO and laser system, is illustrated in Figure 1.

2.2 Laser Launch System

From the optical design point of view, the Laser Launch System (LLS) consists in a pulsed linearly polarized light source extended by a set of lenses. The system is illustated in Figure 2. More specifically, we use a Nd:YAG frequency-doubled laser from Innolas that provides 18 watts at a repetition rate of 10 kHz, for a wavelength of 532 nm with a beam quality factor better than 1.3 TEM_{00}. The pulse duration is about 40 ns at 10 kHz. To shape the beam and launch it on-sky, we use two successive beam expanders. The first one is a commercial off-the-shelf component mounted directly at the output of the laser source. The second one, the "collimator", has been specifically designed to reach 100 mm diameter on sky with high beam quality, and includes the exit lens of the system. The optimization of these two beam expanders is described in 3. The system includes three motorized components. First, a half wave plate adjusts the output beam polarization. Given that the AO module remains fixed while the LLS rotates in altitude with the telescope, the half-wave plate is mounted on a

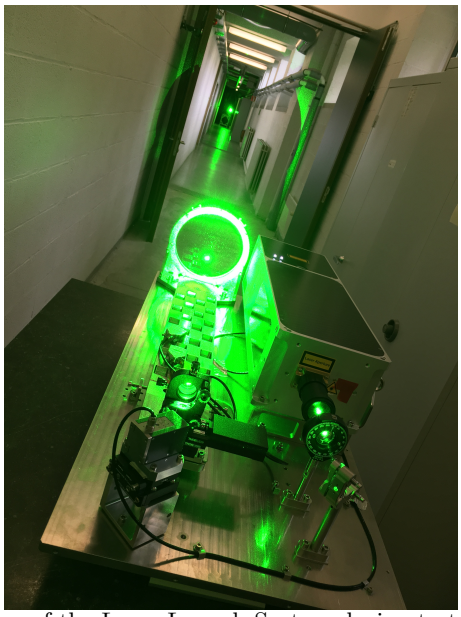

Figure 2. Illustration of the Laser Launch System during test before integration.

motorized rotation stage to automatically adjust the polarization when the altitude angle changes. Second, the fast steering mirror (FSM) driven by the AO-module is used to compensate for small angular deviations and to stabilize the laser guide star on the wavefront sensor. Finally, the diverging lens of the second beam expander is fixed to a motorized translation stage to adjust the focus and compensate for thermal variations. Indeed, while the breadboard is made of Invar, variations of refractive index with temperature require adjustment of the distance between the two lenses of the second beam expander.

2.3 Adaptive Optics System

In a preliminary phase, analytical error budgets and end-to-end simulations were used to defined the optimal system parameters. This is summarized in Section 2.3.1. The AO system was then designed to meet as best as possible those parameters, while using COtS components. The final system is described in Section 2.3.2.

2.3.1 Predicted performances: error budget & end-to-end simulations

Based on analytical expressions, we optimize the subaperture definition (numbers, field-of-view, pixel size) and the LGS altitude. We settled on a 10×10 Shack-Hartmann (SH) array, with 6×6 pixels and ∼1.2″ pixel scale. The actual optical implementation, based on COtS component, is very close to those specifications, see Section 2.3.2. For the LGS altitude, we settled on an altitude of 10km giving us a little bit of margin in term of number of photons at the expense of slightly larger focus anisoplanatism. The current estimate, based on our transmission budget, is approximately 150 photons/ms/subaperture for a gating range of 600m. The resulting analytical error budget performed early on in the project (e.g. see 2, 4) provides a total higher order wavefront rms error of ∼ 145nm, or a Strehl of ∼70% in H-band, assuming a 2″ seeing (r_0=5cm) and a standard Hufnagel-Valley turbulence profile.

In a second phase, we performed end-to-end simulations to provide more accurate performance estimates. To perform those simulations, we use the packages AOtools[5] and Soapy[*]. We included several effects such as e.g., the telescope pupil, realistic influence functions for the deformable mirror, the wavefront sensor detector properties, the laser uplink propagation, and scintillation via Fresnel propagation between the atmospheric layers. The atmospheric seeing and C_n^2 are not well known at Redu, and the only inputs we have are DIMM measurements[4] for a couple of nights taken in 2019 indicating a seeing between 2" and 4". Hence in our baseline, we assume a Hufnagel-Valley profile and simulate 4 different layers. But we also performed sensitivity analyses for different

[*]`https://github.com/AOtools/aotools` and `https://github.com/AOtools/soapy`

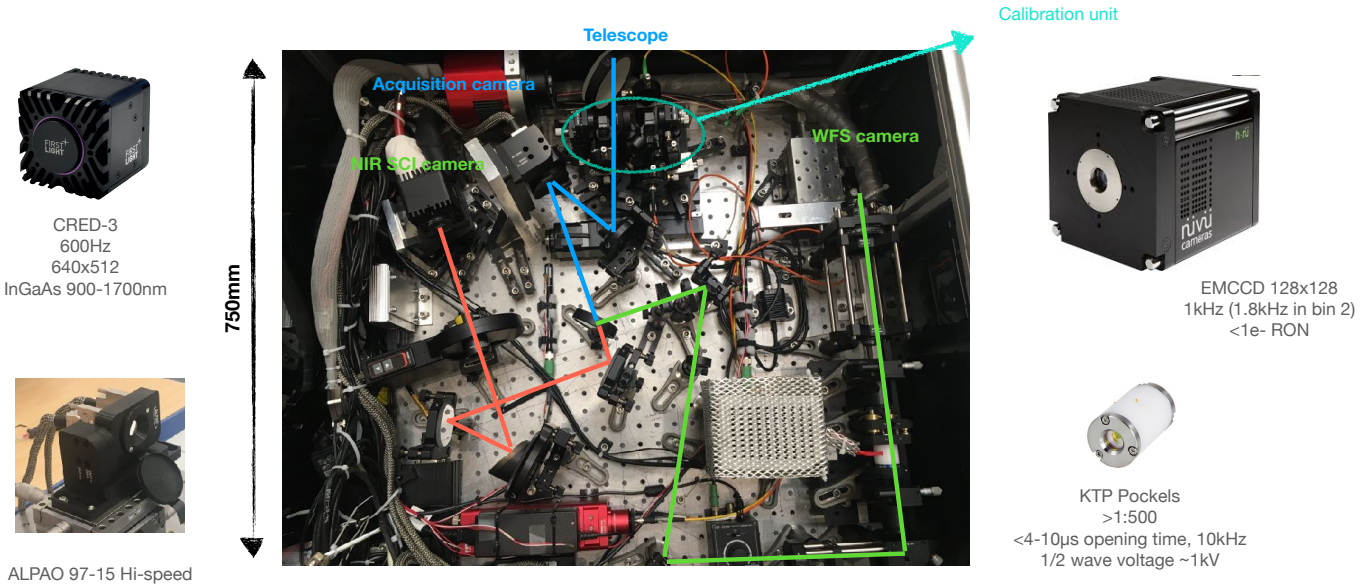

Figure 3. Illustration of the AO instrument. The common path is indicated in blue. The light is then split between the visible (green) and near-infrared (red) by a dichroic. The visible wavefront sensor implement a Shack-Hartmann and include a Pockels cell acting as fast electro-optical shutter synchronized with the LGS. The near-infrared science path consists of a simple imager arrangement and include a set of broad filters (in the 900-1700nm range). It can also act as a fast NGS tip-tilt sensor.

seeing levels, different relative layer contributions, and different servo-lag and measurement errors. More details are given in 4. Because the turbulence will be relatively strong ($r_0 = 5$ cm and below) and our spatial sampling is relatively high ($d = 8$ cm), we expect the flux within our WFS subapertures to vary strongly over time due to scintillation. We therefore performed Fresnel propagation between the atmospheric layers to generate phase and amplitude aberration maps. For a $2''$ seeing, the simulated flux standard deviation between subapertures is about 50%. This strong fluctuation has required further investigation to ensure the loop stability and decent performance. In the end, we obtained a total of about 160 nm rms wavefront error. This is slightly higher but consistent with our initial analytical error budget. When increasing the seeing from $2''$ and $4''$, we progressively see a drop in performance where we no longer reach the diffraction limit at visible wavelength. Using the open to closed-loop FWHM ratio as metric, one see that the maximum gain in resolution - typically above a factor 4 - shifts from the visible ($\lesssim$650nm) for $2''$ to the near-infrared $\gtrsim$1550nm for $4''$ seeing.

2.3.2 AO optical design and integration

The AO and imaging system sits on the Nasmyth platform of the telescope. The instrument is mounted on a standard 750×750mm optical breadboard. A picture of the instrument fully assembled is given in Figure 3.

The light enters the instrument box through a circular aperture leaving the 20-arcmin telescope field-of-view (FoV) unvignetted. After the telescope prime focus, an off-axis parabola (OAP) re-images the pupil on our deformable mirror (DM), a high-speed 97-actuators DM from ALPAO. The reflected and collimated light is then split by our near-infrared dichroic, reflecting the 400-633nm visible light and transmitting the near-infrared (approx. 700-1600nm).

The near-infrared science path is then a simple re-imaging system. First, two reflecting mirrors fold appropriately the beam. Then a second off-axis parabola is used. This parabola has the same optical properties as the first OAP, allowing to almost perfectly compensate any aberration. Then two achromat lenses are used to magnify the beam onto our fast InGaAs camera (900-1700nm), a C-RED3 from First Light with 640×512 15μm pixel size and framerate of up to 600Hz full frame. The path provides a pixel scale of $0.12''$/pix (Nyquist sampling at the shortest wavelength) and a diffraction limited total field-of-view of 1×1.25 arcmin. We place

between the two achromat lenses a filter wheel, with three different broad band filters in the SWIR allowing us to probe the AO performance at different wavelengths.

On the other side, after the dichoic, the visible reflected light is sent to an intermediate field stop focus via one achromat lens and two fold-mirrors. A broadband visible filter is also placed in the path. The field stop provides a $\sim$12.5″ clear aperture matching the subaperture FoV. It prevents any fratricide effects between neighbouring subapertures. After the stop, a 90° OAP recollimates the light. Finally the pupil is re-imaged, after a pupil relay, on a lenslet array which forms the Shack-Hartmann pattern on our WFS camera. The Shack-Hartmann is based on a 10×10 subapertures grid arranged according to the Fried geometry, *i.e.* when projected in the same plane the DM actuators are at the intersects of the subapertures. Each subaperture provides a FoV of 12.4″, which we typically restrict to $\sim$8″ or 8×8 pixels via software. The WFS camera is a Hnü-128AO from Nüvü, a 128×128 EMCCD with sub-electron readout noise operating at up to 1kHz framerate (and up to 1.8kHz with a 2×2 binning).

But SALTO can be operated in NGS or LGS mode. To support the LGS mode, the re-imaging lens after the dichroic in the WFS path is replaced by a convex lens that focuses the LGS light at the field stop. Because we use a Rayleigh laser guide star, we place an electro-optical shutter between the OAP and the pupil relay. Our electro-optical shutter is a KTP Pockels cell placed in-between two crossed polarizers. Its half-wave voltage is approximately 1kV, and it provides a good suppression without any piezo-electric ringing. It allows opening times of $<2\mu$s up to 10μs, or the equivalent of 300m up to 1500m slab. Our baseline is 600m, which would generate a maximum of $\sim$1″ geometrical elongation.

Right before the prime focus of the telescope, a calibration unit and pick-off mirror system mounted on a linear stage can be placed in or out of the beam. When slided in, a large mirror sends the light to our acquisition camera, placed at the telescope prime focus, and covering almost all of the field provided by the telescope. This acquisition camera enables us to test and verify the telescope independently of the AO instrument. It also allows us to perform the NGS and, the more challenging, LGS acquisition.

But the linear stage also hosts our calibration unit. The unit emulates visible and near-infrared natural stars, as well as a 10-km green laser guide star, by matching the f-number and the focus positions. This calibration unit is essential to integrate and align our system, calibrate the AO, and test our module in daytime.

3. REAL-TIME & AO CONTROL

3.1 Real-Time Computer Architecture

The real-time computer (RTC) of SALTO is a custom software development but uses the common data stream format defined in the cacao package.[6] This data stream format includes metadata, pointer to the data held in the shared memory, pointers to semaphores, and additional optional keywords. It allows to perform inter-process communication (IPC) and the implementation supports C/C++ and Python[†]. The basic mechanism is as follows: when a data stream is written by a (single) process, the semaphores are incremented, any downstream process waiting for one of those semaphores will immediately proceed and decrease the semaphore value. More details can be found in 6 and 7.

Our control loop is developed around this data format/IPC mechanism and is illustrated in Fig. 4. By ease of implementation, all the real-time and soft real-time processes have been implemented in Python except for the hardware interfaces that have been implemented either in C or C++. The pipeline itself is described in the next section.

3.2 Adaptive Optics Control and Procedure

The real-time pipeline is triggered as soon as a WFS image as been written in shared memory. At that instant, the WFS slope calculator starts, chopping the different subapertures from the images, and performing a center of gravity measurements. Those two operations are accelerated with the Numba's *just-in-time* compiler. The center of gravity (CoG) is a thresholded CoG with either a dynamical (relative to the peak intensity) or a

[†]for the subpackage itself, see `https://github.com/milk-org/ImageStreamIO`

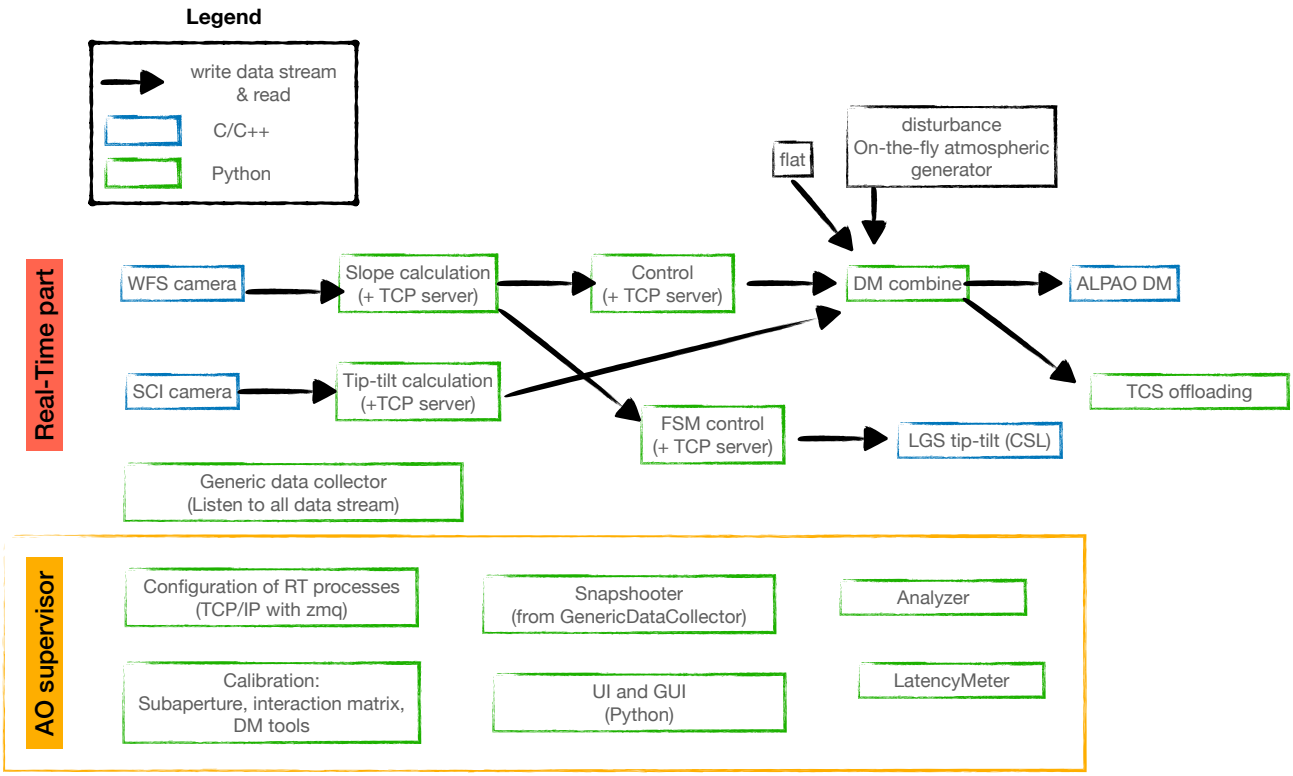

Figure 4. Schematic representation of the SALTO AO software. The real-time loop (but as well as soft real-time processes) are constructed around data stream. Each arrow represents a data stream with its upstream writing and downstream reading by subsequent processes. In LGS mode, because the tip-tilt is measured by the scientific camera, an asynchronous loop is implemented and write tip-tilt commands to one of the DM channels. The LGS tip-tilt is on the other side sent to the LGS FSM. Other processes, including in the AO supervisor, are common to most systems and listed here for illustration purpose.

fixed threshold. The normalization is performed on the the total flux of all the subapertures to minimize noise propagation. After subtraction of the reference slope offsets, the slope vector is written in its shared memory and the respective semaphores are posted, triggering the next computation step performed by the controller worker.

For the controller, we implement a modal leaky-integrator. After computation of the commands we implement the following standard anti-windup strategy: any command exceeding the maximum allowed command by the DM is first clipped, and after sending the mirror commands the actual integrated modal commands are recomputed. The controller writes the DM command in one of the DM channel.

The last steps is a simple combination of the 4 DM channels which allows us to have several channels to address the DM. This includes flat commands, any manual command, the higher-order correction (as computed by the controller), or tip-tilt commands coming from the science camera. This mechanism is also used to introduce real-time disturbance commands for daytime activities.

Using the metadata of the first and last data streams in the real-time pipeline, we can measure the duration of the computation, or approximately 600μs.

In NGS mode, the real-time pipeline is completely described above. The only soft real-time loop that remains is the TCS offloading to avoids too much tip-tilt building up on the DM. In LGS mode, an additional real-time process computes the NGS tip-tilt using the science camera and converts it into a tip-tilt command for the

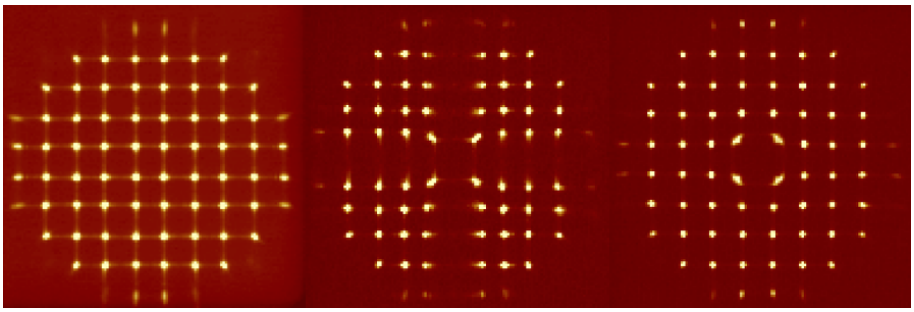

Figure 5. Tuning and verification the Fried geometry between the deformable mirror and the Shack-Hartmann array. (Left) SH pattern measure with our calibration source and flat DM. (Middle) applying a cross on the DM. (Right) pushing only the central actuator.

DM that is written to the appropriate DM channel. In this case, the WFS slope calculator removes the tip-tilt command from the slope vector, and instead sends it to the FSM of the laser system after proper coordinate transformation. Additional soft real-time tasks are envisaged and their implementation will be based on on-sky experience, including time-of-flight adjustment to remove static focus term on the SH, and focus control of the stage in the laser system.

4. CALIBRATION & CHARACTERIZATION

In this section we briefly present some of the key steps performed while calibrating and characterizing our system.

Fried geometry Adjustement of the lenslet array in x, y and in rotation (along the optical axis) was done with a direct feedback from the WFS images. To do so, we applied various shape on the DM and adjusted the alignment to maximize the symmetry of the response. Typical commands that we used are pushing individual actuators (e.g. the central one), or a cross, or a waffle pattern. This simple procedure provides a very good visual feedback and allowed us to interactively aligned our WFS sensor with respect to the deformable mirror. Illustration of the resulting SH images are given in Figure 5.

Modal basis To control our DM with 97 actuators, we generate a modal basis based on theoretical Karhunen-Loeve modes, the measured influence fonctions, and the pupil definition. The construction of the basis essentially follows three steps. First, we construct the theoretical Karhunen-Loève modes orthogonalized on the annular pupil, using AOtools.[5] Then we project this theoretical basis on the influence functions to obtain a first mode-to-command matrix. Finally, we calculate our fitted modal basis and re-orthogonalize it using Cholesky factorization, and perform the same re-orthogonalization on the mode-to-command matrix.

In the process, we perform two sanity checks: we verify that the rms error between our reconstructed modal basis and the theoretical one is as low as possible, and we check that the peak-to-valley actuator displacements remains acceptable. Accordingly we adapt the number of modes of our basis and the regularization applied. Our modal basis used on-sky contains a total of 66 Karhunen-Loève modes for the 97 actuators of our ALPAO DM.

Interaction matrix acquisition The interaction matrix M between the DM and the WFS is acquired using the standard push-pull technique in the modal space. The jth column of the M, containing the WFS slope vector s associated to the jth mode m_j, is computed by

$$M(j) = \frac{s(+Am_j) - s(-Am_j)}{2A} \tag{1}$$

where A is an amplitude vector, which we tune to have a uniform response across all modes. A sanity check is performed by examining the noise covariance matrix, $(M^T M)^{-1}$, and then the reconstructor is computed via pseudo-inversion of the M.

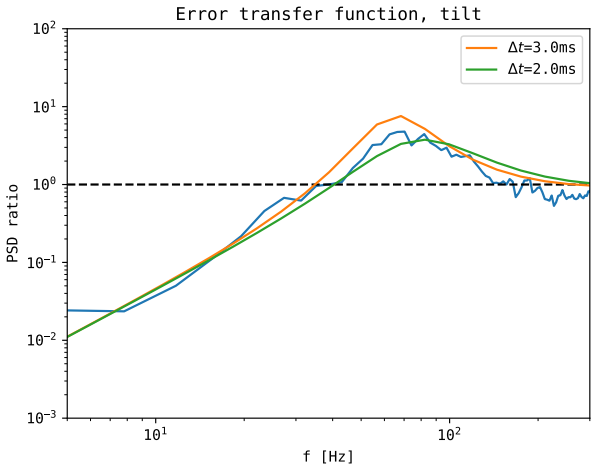

Figure 6. Temporal performance of the AO system by measuring the error transfer function.

Control system model and verification One of the fundamental parameters of the AO system is the time delay τ, which together with the frame time T and the control law $C(s)$ determine the temporal performance of our system. In Section 3 we report a $\sim$600μs delay for the total computation. But this delay does not represent the total latency, as it does not take into account the WFS image acquisition time, and the response time of the DM. To fully characterize the temporal system performance, we model our AO system control loop, evaluate open-loop and closed-loop PSD, and compute the error transfer function. This procedure follows closely what is described in 8, and the AO system model is based on standard techniques (see e.g. 9). The procedure is as follows:

1. acquire open-loop telemetry (typically 20 seconds)
2. acquire closed-loop telemetry (idem)
3. project each time series on a specific modes (e.g. tilt)
4. compute open-loop and closed-loop PSD of the specific mode
5. compare the PSD ratio to a theoretical $|\mathrm{ETF}|^2$ with the time delay as a free parameter

An illustration of one such test is given in Figure 6 where we compare our measurement to theoretical curve with 2 and 3ms total delay. The data are here acquired at 1kHz and with a integrator gain of 0.3. We can see that the measurement is consistent with a pure delay of about 2.5 ms. Out of this delay, $\sim$1ms is used for the WFS camera readout, and $\sim$600μs can be ascribed to the computation. This leaves about 0.9ms which are not precisely identified in our system. One contributor is the dynamic of the DM that is not taken into account in the modeling. The settling time (from 10% to 90%) is measured to be $\sim$0.3ms by the manufacturer. Other contributor are expected to be either a delay in the control electronics of the DM, or in the acquisition of WFS images. With this pure delay, we achieve a bandwidth frequency (defined as the 0dB closed-loop error cut-off frequency) of approximately 35Hz for a gain of 0.3.

Daytime tests For debugging purpose, robustness tests, and characterization, we can inject disturbance on-the-fly onto the DM and try and correct it in closed-loop. Disturbances are injected using one of the DM shared memory channel. To avoid asynchronous clutter when sending data to the DM, the disturbance channel is synchronized with the main higher-order DM channel. Hence, both are forced to be synchronous.

The injected turbulence is generated on-the-fly as a moving phase screens on a 55$\times$55pixels grid, and projected onto the DM space. The generation of phase screens is based on extruded infinite phase screens and use the AOtools package.[5] The Fried parameter, the outer scale, and the wind speed can be changed by the user. The on-the-fly computation takes a little more than 1ms. So injection of disturbance at 1kHz is not fully realistic.

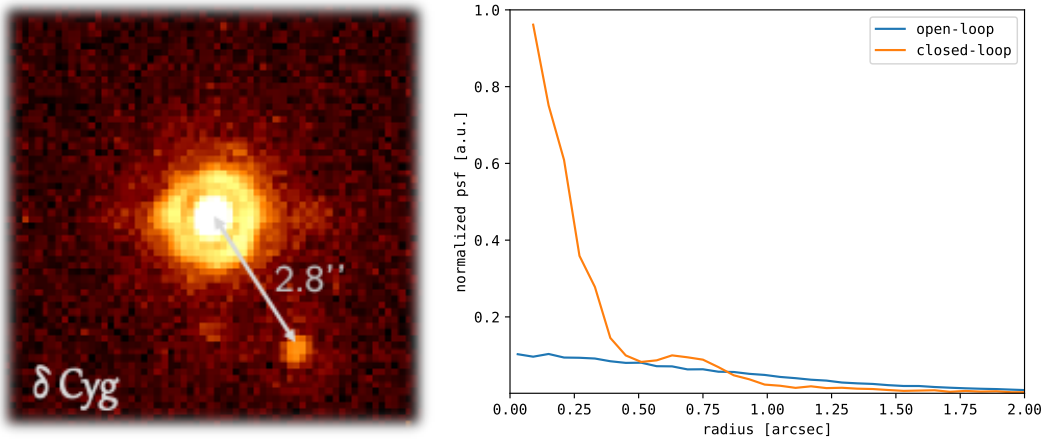

Figure 7. Left: Image with an exposure time of 15 seconds of the delta Cygnus star with delta Cygnus B at about 2.8″. Right: Radial profile in closed-loop (orange) and open-loop (blue) obtained during the first night, based on PSFs of 15 seconds integration time observed at 1.55μm. The peak intensity is boosted here by a factor >6.

5. FROM INTEGRATION TO FIRST ON-SKY OPERATIONS

The bulk of the alignment and integration of the AO system was performed in the first half of 2021. During that period we were still purchasing off-the-shelf components, designing and manufacturing small mechanical parts, characterizing several components, developing the software, and of course performing the fine alignment of the AO system. This AO sub-system phase ended by a first crude functional AO loop in July 2021. In the following month, the system left our ULiège laboratory to be integrated to the telescope at the AMOS premises, and after a few weeks of finalizing the integration, and developing and exercising the AO operation, we performed the first on-sky closed loop test.

Within this first night, we manage to close the AO loop on a NGS, controlling 30 Zernike modes at a 100Hz framerate. The estimated seeing was about 2.5″ but the conditions were relatively steady. We could reach the diffraction limit going from $\sim$ 2″ in seeing-limited conditions to 0.4″ at 1.55μm. The following second and third nights were devoted to streamline the AO operations including communication with the telescope control system, improving the alignment between the AO instrument and the telescope, and several control aspects. An illustration of the PSF obtained by observing delta Cygnus is illustrated in Figure 7. The image is obtained at 1.55μm for a total integration time of 15 seconds. The radial profile also illustrated shows a gain of >6 times in peak intensity.

Various hardware and software improvements were carried out and implemented in the following months. Laser system integration continued through early 2022. After a late deliver, the Pockels cell was tested and integrated to the AO instrument. Subsequently functional laser tests were performed on-sky in April 2022 from the integration hall at Liège, see a picture in Figure 8. During that night, we exercised the laser operation, driving the FSM mirror and adjusting the optical alignment and the laser focus, and finally performed a first acquisition onto the WFS camera. But, without the authorization to propagate at full power, we had too little flux to attempt to close the loop on the LGS.

The full system has been disassembled from the AMOS premises and shipped to Redu Space Services early June 2022. The system is now fully installed at Redu, see Figure 8, and we are currently performing the last sub-system tests before resuming on-sky tests. In particular we will be able to use the laser at its full power and commission the LGS operations. Activities are currently planned until end of 2022, with the objective to demonstrate LGS-AO operation and to characterize the performance in both NGS and LGS modes.

ACKNOWLEDGMENTS

The authors acknowledge the support from the Walloon region of Belgium through the program Skywin (project SALTO). OA thanks the Belgian national funds for scientific research (FNRS).

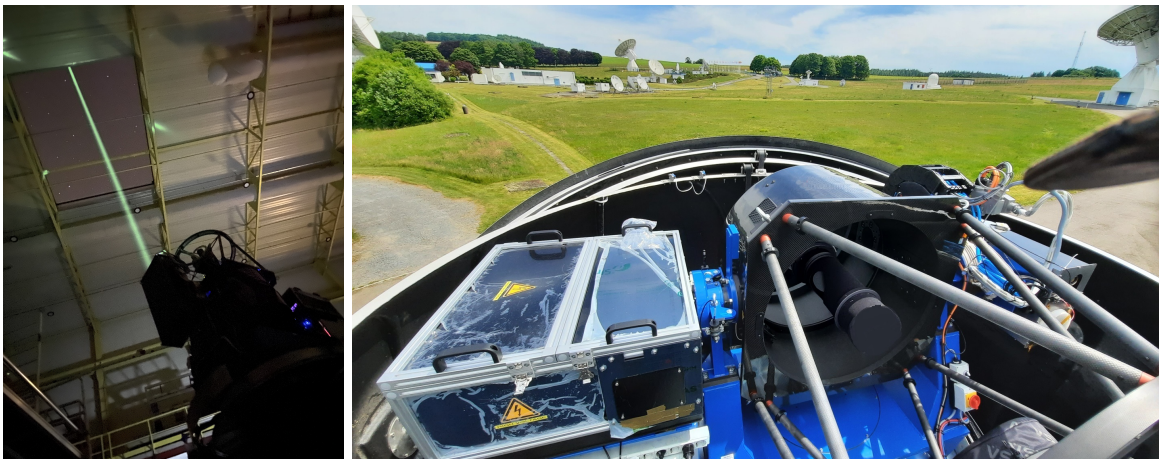

Figure 8. Left: Low power laser propagation test at Liège, with SALTO in its integration hall at AMOS. Right: Recent installation of SALTO at Redu Space Services.

REFERENCES

[1] Baranec, C., Ziegler, C., Law, N. M., Morton, T., Riddle, R., Atkinson, D., Schonhut, J., and Crepp, J., "Robo-AO Kepler Planetary Candidate Survey. II. Adaptive Optics Imaging of 969 Kepler Exoplanet Candidate Host Stars," **152**, 18 (July 2016).

[2] Orban de Xivry, G., Absil, O., and Moreau, V., "A sharp future for the 3.6-m DOT? The power of adaptive optics for medium size telescopes," *Bulletin de la Societe Royale des Sciences de Liege* **88**, 55–64 (Oct. 2019).

[3] Clermont, L., Languy, F., and Georges, M., "Afocal combinations and focus control for laser launch telescopes," *Journal of Astronomical Telescopes, Instruments, and Systems* **6**, 034003 (July 2020).

[4] Orban de Xivry, G., Absil, O., Lismont, M., Moreau, V., Languy, F., and Vanhoenacker-Janvier, D., "Preliminary design of SALTO: the Belgian adaptive optics demonstrator," in [*Adaptive Optics Systems VI*], Close, L. M., Schreiber, L., and Schmidt, D., eds., *Society of Photo-Optical Instrumentation Engineers (SPIE) Conference Series* **10703**, 1070338 (July 2018).

[5] Townson, M. J., Farley, O. J. D., Orban de Xivry, G., Osborn, J., and Reeves, A. P., "AOtools: a Python package for adaptive optics modelling and analysis," *Optics Express* **27**, 31316 (Oct. 2019).

[6] Guyon, O., Sevin, A., Gratadour, D., Bernard, J., Ltaief, H., Sukkari, D., Cetre, S., Skaf, N., Lozi, J., Martinache, F., Clergeon, C., Norris, B., Wong, A., and Males, J., "The compute and control for adaptive optics (CACAO) real-time control software package," in [*Adaptive Optics Systems VI*], Close, L. M., Schreiber, L., and Schmidt, D., eds., *Society of Photo-Optical Instrumentation Engineers (SPIE) Conference Series* **10703**, 107031E (July 2018).

[7] Guyon, O., Sevin, A., Ferreira, F., Ltaief, H., Males, J., Deo, V., Gratadour, D., Cetre, S., Martinache, F., Lozi, J., Vievard, S., Fruitwala, N., Bos, S., and Skaf, N., "Adaptive optics real-time control with the compute and control for adaptive optics (Cacao) software framework," in [*Society of Photo-Optical Instrumentation Engineers (SPIE) Conference Series*], *Society of Photo-Optical Instrumentation Engineers (SPIE) Conference Series* **11448**, 114482N (Dec. 2020).

[8] Poyneer, L. A., Palmer, D. W., Macintosh, B., Savransky, D., Sadakuni, N., Thomas, S., Véran, J.-P., Follette, K. B., Greenbaum, A. Z., Mark Ammons, S., Bailey, V. P., Bauman, B., Cardwell, A., Dillon, D., Gavel, D., Hartung, M., Hibon, P., Perrin, M. D., Rantakyrö, F. T., Sivaramakrishnan, A., and Wang, J. J., "Performance of the Gemini Planet Imager's adaptive optics system," **55**, 323 (Jan. 2016).

[9] Madec, P. Y., "Control techniques," in [*Adaptive Optics in Astronomy*], Roddier, F., ed., 131 (1999).